The Southern Hemisphere Sudden Stratospheric Warming in September 2019 and its predictions in S2S Models

Jian Rao[1,2], Chaim I. Garfinkel[1], Ian P. White[1], and Chen Schwartz[1]

[1]Fredy and Nadine Herrmann Institute of Earth Sciences, The Hebrew University of Jerusalem, Edmond J. Safra Campus, Givat Ram Jerusalem 91904, Israel

[2]Key Laboratory of Meteorological Disaster, Ministry of Education (KLME) / Joint International Research Laboratory of Climate and Environment Change (ILCEC) / Collaborative Innovation Center on Forecast and Evaluation of Meteorological Disasters (CIC-FEMD), Nanjing University of Information Science and Technology, Nanjing 210044, China

Submitted to *Journal of Geophysical Research – Atmospheres*

(March 2020)

Corresponding author: Dr. Jian Rao, jian.rao@mail.huji.ac.il

Key Points:

- A SH SSW happened in September 2019, with westerly winds at 10 hPa, 50°S reversed on 16 September.
- This SH SSW appeared during several favorable conditions, including easterly QBO winds, solar minimum, positive IOD, and warm SST anomalies in the central Pacific.
- The predictive limit to this SSW is ~18 days in some S2S models, but models forecast a faster tropospheric response to the SSW.

Abstract

A sudden stratospheric warming (SSW) happened in September 2019 in the Southern Hemisphere (SH) with winds at 10hPa, 60°S reaching their minimum value on September 18. Using multiple datasets and real-time predictions from 11 subseasonal to seasonal (S2S) models, the evolution, favorable conditions, and predictability for this SSW event are explored. The September 2019 SSW happened during several favorable conditions, including easterly equatorial quasi biennial oscillation (QBO) winds at 10hPa, solar minimum, positive Indian Ocean Dipole (IOD) sea surface temperatures (SST), warm SST anomalies in the central Pacific, and a blocking high near the Antarctic Peninsula. With these favorable initial and boundary conditions, the predictive limit to this SSW is around 18 days in some S2S models, and more than 50% of the ensemble members forecast the zonal wind deceleration in reforecasts initialized around 29 August. A vortex slowdown in evident in some initializations from around 22 August, with a forecast–reanalysis pattern correlation <0.5, while initializations later than 29 August capture the wave-like pattern in the troposphere and the subsequent stratospheric evolution. The ensemble spread in the magnitude of the vortex deceleration during the SSW is mainly explained by the ensemble spread in the magnitude of upward propagation of waves in the troposphere and in the stratosphere, with an underestimated tropospheric wave amplitude leading to a too-weak weakening of the vortex. The September 2019 SH SSW did not show a near-instantaneous downward impact on the tropospheric southern annular mode (SAM) in late September and early October 2019. The Australian drought and hot weather in September possibly associated with the positive IOD might have been exacerbated by the negative SAM in October and later months due to the weak stratospheric polar vortex. However, models tend to forecast a near-instantaneous tropospheric response to the SSW.

Key words: Sub-seasonal to seasonal (S2S); Sudden stratospheric warming (SSW); Southern Hemisphere (SH); predictability; September 2019

1. Introduction

Extreme stratospheric events such as sudden stratospheric warmings (SSWs) have downward impacts that can reach down to the surface in both Northern (Baldwin & Dunkerton, 1999, 2001; Hitchcock & Shepherd, 2013; Domeisen et al., 2020a, 2020b; Rao et al., 2020) and Southern Hemispheres (Gillett & Thompson, 2003; Thompson et al., 2005; Polvani et al., 2011; Waugh et al., 2015; Lim et al., 2018) on both subseasonal and decadal timescales. The stratospheric polar vortices in both hemispheres are strong westerly winds that encircle the Poles and become strongest in the winter half of the year (Kodera & Kuroda, 2002; Waugh et al., 2017). In the Northern Hemisphere (NH), midwinter SSWs occur six to seven times every decade (Charlton & Polvani, 2007; Butler et al., 2015; White et al., 2019). Although generally not as spectacular as SSW events in the NH, the polar stratosphere in the Southern Hemisphere (SH) can also be disturbed (Allen et al., 2006; Lim et al., 2019; Rao & Ren, 2020). The NH polar vortex is mainly perturbed during boreal midwinter and spring (Waugh et al., 2017), while the SH polar vortex tends to be perturbed episodically during austral spring to early summer (Randel, 1988; Kuroda & Kodera, 1998; Hio & Yoden, 2005). The SH stratospheric polar vortex perturbation can superimpose on the seasonal evolution of the vortex, viewed as an earlier or later transition from the wintertime circulation to the summertime circulation (Byrne & Shepherd, 2018; Butler & Gerber, 2018; Lim et al., 2019).

Variability of upward-propagating planetary waves perturbs the stratospheric polar vortex, which can couple with the troposphere and serve as a potential source of sub-seasonal to seasonal (S2S) predictability of surface weather and climate (Baldwin et al., 2003; Charlton et al., 2003; Byrne & Shepherd, 2018; Lim et al., 2018). For example, the negative stratospheric annular mode associated with an SSW can cause sustained impacts on surface climate via excitation of the negative tropospheric Southern or Northern Annular Modes (SAM or NAM) in both hemispheres (Baldwin & Dunkerton, 1999; Baldwin et al., 2003; Sigmond et al., 2013). Since the stratosphere usually has a longer memory than the troposphere, a downward-propagating signal from the stratosphere can be used to enhance predictability of surface weather on the S2S timescale in both hemispheres (Sigmond et al., 2013; Tripathi et al., 2015, 2016).

On the interannual to decadal timescales, similar to the variation of the NH stratospheric polar vortex, the SH stratospheric polar vortex can also be dynamically affected by the El Niño–Southern Oscillation (ENSO) (Hurwitz et al., 2011; Zubiaurre & Calvo, 2012; Rao & Ren, 2020), the quasi-biennial Oscillation (QBO) (Baldwin & Dunkerton, 1998; Naito, 2002), solar cycle (Kodera & Kuroda, 2002; Kuroda & Kodera, 2005), and ozone depletion (Polvani et al., 2011; Kidston et al., 2015; Waugh et al., 2015). In the SH the influence stemming from the aforementioned forcings can weaken or strengthen the circumpolar jet, which in turn causes a meridional shift of the tropospheric jet and therefore variations in the tropospheric SAM (Arblaster & Meehl 2006; Son et al., 2010). Therefore, ENSO, the QBO, solar cycle and ozone depletion or recovery may provide some predictability for SH winds and the SAM especially on longer timescales. In contrast, prediction on the S2S timescale depends not only on boundary conditions, but also on initial conditions (Kistler et al., 2001; Tripathi et al., 2015).

Waugh et al. (1998) found that the prediction skill of the lower stratosphere (50 hPa) for the SH vortex at a week lead time was comparable to the tropospheric prediction skill at a 3-day lead time when the SH vortex was undisturbed. Lahoz (1999) also found that the lower stratosphere is more predictable than the middle troposphere in the UKMO unified forecasting model, but the SH winters seem to be less predictable than NH winters (also see Figure 5 in Kistler et al., 2001; Figure 2 in Gerber et al., 2012). In both the NH and SH, a decent stratosphere in the forecasting model can enhance tropospheric prediction (Roff et al., 2011; Gerber et al., 2012). In austral spring when SH stratosphere-troposphere coupling is strongest (Thompson et al., 2005; Rao & Ren, 2020), the extended-range (or S2S) prediction skill in the troposphere and near surface may be enhanced with a well-resolved stratosphere (Roff et al., 2011; Son et al., 2013).

Major midwinter SSWs rarely occur in the SH (only one major midwinter SSW occurred in the SH in 2002), largely because of weak land-sea contrast and small planetary wave amplitudes in the SH (Ren & Cai, 2008; Chen et al., 2019; Rao & Ren, 2020). Only two SSWs were observed in the SH, one in September 2002 (Allen et al., 2003; Tripathi et al., 2016), and the other in September 2019 (Yamazaki et al., 2020). Since the SH SSW was observed in September 2002, there have been a large amount of reports for predictability of this event (Simmons et al., 2005; Allen et al., 2006; Taguchi, 2018). Simmons et al. (2005) compared three NH sudden warmings (January 1958, February 1979, and February 2003) and the September 2002 SH warming and found a similar level of forecast skill for those events in the ECMWF model. Using a high-top version (upmost level: 0.005 hPa) of the Navy Operational Global Atmospheric Prediction System (NOGAPS) model, Allen et al. (2006) also explored predictability of the September 2002 SH warming. This unprecedented stratospheric warming event can be forecasted 6 days in advance, and the main features of the westerly reversal, planetary wave pulse, and splitting of the polar vortex could be well forecasted in the NOGAPS initializations. Similar to some NH SSWs (e.g., January 2009, February 2018), the September 2002 SH SSW experiences rapid wind decelerations (Taguchi, 2018; Rao et al. 2018, 2019a) and can only be forecasted less than two weeks in advance.

However, the prediction of the second SH warming event on record has not been explored, and the possible downward impact of this event on the SH surface weather is not yet reported. Since the World Climate Research Program and the World Weather Research Program initiated the S2S prediction project in 2013, three SSWs have been observed, including the NH events in mid-February 2018 (Karpechko et al., 2018; Rao et al., 2018) and early January 2019 (Rao et al., 2019b, 2020), and the SH event in September 2019 (Yamazaki et al., 2020). This study considers the predictability of the September 2019 SH event using the real-time predictions from 11 S2S models. Different from the September 2002 vortex split SSW, the September 2019 SSW was a vortex displacement event. We mainly focus on the following two questions: (1) What were the main tropospheric and stratospheric drivers of the September 2019 SH SSW? (2) How predictable is this event?

The structure of the paper is organized as follow. Following this section, section 2 introduces the S2S models and methods. Section 3 explores the evolution of the September

2019 SH SSW. Section 4 presents the favorable circulation conditions for the occurrence of an SSW. Prediction of this SSW in multiple S2S models is shown in section 5. In this section, the possible surface impact of this SSW is also discussed. Finally, conclusions and a discussion are provided in section 6.

2 S2S real-time predictions, data, and methods

2.1 S2S models and real-time predictions

All real-time forecasts initialized in the month before the September 2019 SH SSW event from the 11 models participating in the S2S project are used in this study. All the real-time predictions for those models are collected by the ECMWF (https://confluence.ecmwf.int/display/S2S). The 11 S2S models are the Australian Bureau of Meteorology (BOM), China Meteorological Administration Beijing Climate Centre (CMA-BCC), Environment and Climate Change Canada (ECCC), European Centre for Medium-range Weather Forecasts (ECMWF), Hydro-Meteorological Centre of Russia (HMCR), Institute of Atmospheric Sciences and Climate National Research Council of Italy (ISAC-CNR), Japan Meteorological Agency (JMA), Korea Meteorological Administration (KMA), Météo-France/Centre National de Recherche Meteorologiques (METEO), National Centers for Environmental Prediction (NCEP), and United Kingdom Meteorological Office (UKMO). ECCC, HMCR, ISAC-CNR, JMA, and METEO are initialized once a week; BOM and ECMWF are initialized twice weekly; CMA-BCC, KMA, NCEP, and UKMO are initialized every day. Each initialization has multiple ensemble members, and the ensemble size is also different among models. The ensemble size for a particular initialization is 4 in three models (CMA-BCC, KMA, UKMO), 16 in NCEP, 20 in HMCR, 21 in ECCC, 33 in BOM, 41 in ISAC-CNR, 50 in JMA, and 51 in two models (ECMWF, METEO). The integration time is also different: about one month in three models (ECCC, ISAC-CNR: 32 days; JMA: 33 days), ~1.5 months in two models (NCEP: 44 days; ECWMF: 46 days), and two months in the remaining six models (CMA-BCC, KMA, UKMO: 60 days; HMCR, METEO: 61 days; BOM: 62 days).

2.2 Data

The daily and monthly NCEP/NCAR (Kalnay et al., 1996) and JRA-55 (Kobayashi et al., 2011) reanalyses are used in this study as the reference. Because the evolution of the September 2019 SSW in the two reanalyses are nearly the same, only the NCEP/NCAR is shown as a verification. All forecasts from S2S models are interpolated to 2.5° × 2.5° (latitude × longitude) horizontal resolution. To explore the potential predictability source of this SSW, favorable conditions are also analyzed with the following datasets: (1) the multivariate Madden-Julian Oscillation (MJO) daily time series provided by the Australian Bureau of Meteorology (http://www.bom.gov.au/climate/mjo); (2) the monthly mean time-series of the ENSO index derived from the COBE sea surface temperature (SST) dataset compiled by the Japanese Meteorological Agency and redistributed by ESRL, NOAA (https://www.esrl.noaa.gov/psd/data/gridded/data.cobe.html); (3) the quasi biennial oscillation (QBO) time series shared by Berlin Free University (https://www.geo.fu-berlin.de/en/met/ag/strat/produkte/qbo/index.html); (4) the combined 10.7cm solar flux by

NOAA (ftp://ftp.ngdc.noaa.gov/STP/space-weather/solar-data/solar-features/solar-radio) from 1979–2017 and by Natural Resources Canada (https://www.spaceweather.gc.ca/solarflux/sx-5-mavg-en.php) from 2018–2019 to denote the 11-year solar cycle. Based on those datasets, it will be shown that the observed warm SST anomalies in central Pacific, the cold SST anomalies in the tropical East Indian Ocean, the easterly QBO at 10 hPa (QBO10), and the solar minimum in the 2019 austral winter are favorable conditions for the September 2019 SH SSW.

2.3 Methods

In the NH, SSW events are usually selected using a strict benchmark: a major SSW is defined if the zonal-mean zonal winds at 60°N and 10hPa reverse from westerlies to easterlies (Charlton & Polvani, 2007; Butler et al., 2015), and the zonal mean temperature gradient between 60°N and the North Pole reverses. Similar definition can be used for the SH SSW event, but with a less strict benchmark. A SH SSW event is identified when the zonal-mean zonal winds at 60°S and 10hPa decrease to ≤ 20 m/s. Based on this threshold, the SSW onset date at 10hPa is 16 September 2019. Note that zonal winds at 50°S, 10hPa reversed on 16 September16 2019 (Figure 1).

Because the eddy heat flux is proportional to the vertical component of the EP flux (F_z), we also calculate the eddy heat flux ($[V'T']$) at 500 hPa and 100 hPa to represent upward propagation of planetary waves from the middle and upper troposphere, respectively.

To assess the prediction of circulation patterns and to quantify model performance, the pattern correlation coefficient (PCC) between forecasts and the reanalysis for height anomalies (H) is utilized, $\mathrm{PCC}(t) = \frac{\sum_{i=1}^{n} w(i)[H_{\mathrm{FC}}(i,t)-\overline{H_{\mathrm{FC}}(t)}][H_{\mathrm{RE}}(i,t)-\overline{H_{\mathrm{RE}}(t)}]}{\sqrt{\sum_{i=1}^{n} w(i)[H_{\mathrm{FC}}(i,t)-\overline{H_{\mathrm{FC}}(t)}]^2}\sqrt{\sum_{i=1}^{n} w(i)[H_{\mathrm{RE}}(i,t)-\overline{H_{\mathrm{RE}}(t)}]^2}}$. In the PCC formula, t denotes the forecast day t (t = 0 denotes the initial day), i is the spatial grid index, n is the total number of spatial grid points in the southern extratropics (20–90°S). The subscript "FC" denotes the forecast, and "RE" denotes the reanalysis. The overbars in the PCC formula denote spatial averages, including the $w(i)$ (cosine of latitude) weighting, $\overline{H(t)} = \frac{\sum_{i=1}^{n} w(i)H(i,t)}{\sum_{i=1}^{n} w(i)}$. The PCC is also employed to attribute the predictability source of the circulation pattern for the September 2019 SH SSW.

To assess the probability of successful forecast in the multiple-member ensemble, the SSW hit ratio is also used, $r = \frac{M}{N} \times 100\%$. N is the number of total ensemble members, and M is the number of the members that forecast $[U]_{10\mathrm{hPa/60S}}$ decelerated to < 20m/s on any day of 14–18 September 2019 (i.e., a maximum error of two days on both sides is allowed for the deceleration timing).

3 Observed evolution of the September 2019 SSW

Evolutions of the Antarctic polar cap geopotential height at 10hPa ($[H]_{10\mathrm{hPa/SP}}$), the polar cap temperature at 10hPa ($[T]_{10\mathrm{hPa/SP}}$), and zonal-mean zonal wind at 60°S (50°S) and 10

hPa ($[U]_{10hPa/60S}$) from 17 August–16 October are shown in Figure 1. The climatological southern circumpolar westerlies are ~80 m/s (Figure 1c), and the observed wind deceleration amplitude in mid-September 2019 exceeded 60 m/s (80 m/s decelerating to below 20 m/s). In contrast, the climatological northern circumpolar westerlies are ~30 m/s (Figures 1d, 1f), and the observed maximum easterlies for some strong NH SSWs are ~-20 m/s (Rao et al., 2019a). Therefore, the observed southern circumpolar zonal wind anomalies for the SH September 2019 SSW are even larger than some NH major SSWs (a deceleration of -60 m/s compared to -50 m/s). The SSW onset date varies with the threshold, which does not affect the assessment of predictions in S2S models if all models are evaluated with the same threshold. Comparing the September 2002 SSW and the September 2019 SSW, the Antarctic polar cap height and temperature (Figures 1a, 1b) are of similar values relative to their climatology, although the circumpolar zonal wind at 60°S only for the former event reversed from westerlies to easterlies (Figure 1c). However, the westerly winds at 50°S reversed to easterly winds on 16 September 2019 (Figure 1e). Following the two SSWs, a weak polar vortex persists until the final warming: the westerlies in the post-SSW period bottomed-out below 20 m/s.

Figure 2 shows evolution of geopotential height, temperature and zonal wind during the September 2019 SSW. Following the SSW onset, the maximum height anomalies at 10hPa reached 2000 gpm in the Antarctic, while negative height anomalies occurred in the tropical stratosphere (Figure 2a). Large positive height anomalies formed 20 days before the SSW onset (from 27 August), and increased in the following >20 days (Figure 2b). After the onset, the positive polar cap height anomalies (or negative SAM) in the stratosphere had a long lifetime in the following months. The Antarctic troposphere was dominated by negative height anomalies before onset, and the negative stratospheric SAM did not propagate downward instantly after the SSW onset (Figure 2c). This might suggest that the tropospheric response to SSW also depends on the preexisting tropospheric circulation conditions (Gerber et al., 2009; Garfinkel et al., 2013; Hitchcock & Simpson, 2014; White et al., 2019). This SSW did not have a rapid impact on the troposphere, although there was a short and weak pulse of a negative SAM (9–15 October).

Similarly, warm Antarctic temperature anomalies began to form on 27 August, then increased in the following >20 days (Figures 2d, 2e). The maximum warming was centered in the Antarctic stratospheric around 16 September (Figure 2d), and the warm anomalies persisted for >20 days in high latitudes (Figure 2e). Consistent with the polar cap height evolution, the Antarctic temperature anomalies also showed a downward propagation from the stratosphere to upper troposphere. The near surface temperature anomalies oscillated between positive and negative and did not show any preference to the sign (Figure 2f).

This minor SSW event was accompanied by a strong westerly deceleration, denoted by large easterly anomalies in the subpolar region (Figures 2g–2i). The maximum easterly anomalies reached ~60 m/s around 16 September (Figure 2g). Easterlies are also evident in the tropical stratosphere, which are associated with the easterly QBO10. Although easterlies were not observed at 60°S, they appeared at 50°S with the zonal wind transition on 16 September (Figure 2h). Negative easterly anomalies at 10hPa began to appear on 27 August but developed

throughout the stratosphere (Figure 2i). Before the SSW onset, westerly anomalies appeared in the troposphere, which might obscure the downward impact of the September 2019 SSW. In summary, the September 2019 SH SSW was not observed to show any substantial impact on the troposphere in late September and early October 2019 after its onset, although it may have impacted Australian dry and wildfire conditions in November 2019 (Lim et al., 2019).

4 Possible predictability sources of the tropospheric and stratospheric circulation for the September 2019 SSW

4.1 Stratospheric predictability sources

The predictive limit for the 2019 major SSW event in the NH has been recently found to be longer than the average, likely due to preceding tropical tropospheric and stratospheric conditions that are favorable for a vortex weakening (Rao et al., 2020). Here, we examine whether similar atmospheric conditions were present before the 2019 sudden warming in the SH polar stratosphere, thus potentially contributed to enhanced predictability of this event. Figure 3 shows the austral winter-mean QBO10 index from Berlin Free University and the austral winter solar flux at 10.7cm (SF10.7) from NOAA and Natural Resources Canada, as well as the composite geopotential height patterns at 500 hPa in the following September. The extremely weak Antarctic stratospheric polar vortex in September 2019 happened following the easterly QBO10 and solar minimum in the preceding austral winter (Figures 3a, 3b). It is shown that the September 2002 SH SSW also appeared following the easterly QBO10 (Figure 3a). However, the September 2002 SSW appeared during the solar maximum, while the September 2019 SSW appeared during the solar minimum.

To attribute the possible predictability sources of the stratospheric circulation pattern in September 2019, the observed eddy height anomaly pattern at 10 hPa in September 2019 and the composite height patterns in September for easterly QBO10 phases and solar minima are also shown in Figure 3. Considering that the observed anomalies were much larger than earlier and later sub-periods in Figure 1, it is more reasonable to take the entire September mean than any sub-period. An anomalous wave-1-dominated height pattern was observed to enhance the climatological waves (purple contours) in September 2019, favoring displacement of the polar vortex toward the Antarctic Peninsula (Figure 3c). The positive extrema of the wave-1 pattern were situated south of Australia, while the negative extrema were located over the Antarctic Peninsula. Such a circulation anomaly pattern was likely explained by the easterly QBO10 and the solar minimum (Figures 3d, 3e). As in the NH, the Holton-Tan relationship is also identified for the SH (Baldwin & Dunkerton, 1998) but optimized using equatorial wind at lower pressure level (10 hPa here). The easterly QBO10 on average excites a positive height center over the South Indian Ocean, with a PCC of 0.35 with the observed circulation pattern in Figure 3c (Figure 3d). In contrast, the solar minimum on average excites a negative height center over South Atlantic Ocean, with a PCC of 0.45 (Figure 3e).

4.2 Tropospheric predictability sources

Tropical convection anomalies associated with the Madden-Julian Oscillation (MJO) have been shown be a major source for an improved predictability of the extratropics in both

hemispheres (Vitart, 2014; Garfinkel & Schwartz, 2017; Yang et al., 2017; Rao et al., 2020). Now we explore the possibility that MJO-related convection anomalies contributed to the prediction skill of the 2019 SSW event in the SH. The MJO evolution (Wheeler & Hendon, 2004) during July–September 2019 and the associated convection activity denoted by the outgoing longwave radiation (OLR) anomalies and the extratropical height anomalies in four sub-periods are shown in Figure 4. The largest responses of the SH stratospheric polar vortex to MJO appears ~30 days after the MJO phase 1 (Yang et al., 2017). However, the MJO amplitude in August and early September 2019 was fairly weak (Figure 4a), and the OLR anomalies over tropical Indian and Pacific Oceans were not well organized in the four sub-periods (Figures 4c–4f). The convection in the eastern tropical Indian Ocean is suppressed in the four sub-periods (denoted by positive OLR anomalies), and the convection in the tropical western Indian Ocean is weakly enhanced for all sub-periods (see the two green boxes over the tropical Indian Ocean).

These stable convection anomalies are not associated with a typical MJO, but with the local SST anomalies in the tropical Indian Ocean (Figure 4b). A moderate El Niño event developed in the 2018/2019 boreal winter (Rao et al., 2019b), and gradually decayed in the following 2019 boreal summer (austral winter). Warm SST anomalies remained in the central Pacific Niño4 region, which have been shown to more strongly affect the SH vortex than the eastern Pacific ENSO (Hurwitz et al., 2011; Zubiaurre & Calvo, 2012; Rao & Ren, 2020). The central Pacific warm SST anomalies appear to have led to an enhanced precipitation in western tropical Pacific in the last 10 days before the SSW (Figure 4f). In the tropical Indian Ocean, a SST anomaly dipole (i.e, a positive IOD) was observed, which is consistent with the local convection dipole in the four sub-periods. Therefore, it might be concluded that the extratropical circulation pattern is more associated with the SST anomalies than the MJO. The SST anomalies can persist for a much longer time than the MJO, and the extratropical circulation pattern was persistent over the four sub-periods, especially the high anomaly center over the Antarctic Peninsula and the low anomaly center over the South Indian Ocean (Figures 4c–4f). Those two centers are just located in the climatological ridge over the southeast Pacific and the climatological trough over the South Atlantic Ocean (purple contours in Figures 4c–4f).

The combination of a positive IOD and a central Pacific El Niño-like forcing might explain the observed high anomalies (associated with the preceding blocking) extended from the Antarctic Peninsula to the South Atlantic Ocean. The role of antecedent blocking in forcing a SH vortex weakening has been reported (Allen et al., 2006; Wooling et al., 2010). For example, Allen et al. (2006) found that the blocking high over the South Ocean leads to enhanced upward wave flux, which forced the September 2002 SH SSW. The same forcing was also observed before the September 2019 SSW.

Figure 5 shows the time series of the austral winter-mean IOD index and Niño4 (5°S–5°N, 160°E–150°W) index, as well as the composite tropospheric height patterns in September. The IOD index is the difference in SST anomalies between the IOD west (50–70°E, 10°S–10°N) and east regions (90–110°E, 10–0°S). A typical positive IOD event appeared in the 2019

austral winter (Figure 5a), and warm SST anomalies remained in the central Pacific (Figure 5b). No positive IOD event was observed for the September 2002 SSW event, but warm SST anomalies also prevailed in the central Pacific for the 2002 event (Figures 5a, 5b). The net effect is that a wave-like pattern was observed in September 2019 (Figure 5c), although only wave-1 propagated upward to disturb the polar vortex (Figure 3c). The high center near the Antarctic Peninsula and the low center over the South Indian Ocean enhanced the climatological waves (purple contours in Figure 5c, dominated by wave-1). The positive IOD forces a wave train-like circumglobal pattern, with the high and low centers in phase with the observed height pattern in September 2019 (Figure 5d). The PPC between the height response to IOD and the observed height pattern in the SH extratropics is 0.52, highlighting the role of the IOD SST forcing. Similarly, warm SST anomalies in central Pacific also force a similar circumglobal height pattern (Figure 5e). The highly similar response of the extratropical troposphere to IOD and ENSO might indicate their entanglement, because most of the positive IOD events during the austral winter happen in the El Niño decaying phase.

5 Prediction of the September 2019 SSW in S2S models

5.1 Prediction of the SSW hit ratio and zonal-mean zonal wind evolution

Figure 6 considers the success of each S2S model to forecast the SSW. Specifically, it shows dates in which reforecasts are available (filled grid) and their ensemble size (number in the filled grid). The color denotes the SSW hit ratio (i.e., the ratio between the ensemble members that forecast the deceleration of $[U]_{10\text{hPa}/60\text{S}}$ to <20 m/s around 16 September 2019 and the total number of ensemble members). It is clear that the maximum predictive limit exceeds 18 days in five models (i.e., ECMWF, JMA, KMA, NCEP, and UKMO) if at least a hit ratio of 50% is required. Therefore, this minor SSW also seems to be more predictable than most NH SSW events, perhaps due to the external forcings (easterly QBO10, solar minimum, moderate central Pacific El Niño, positive IOD, and Antarctic Peninsula blocking) that were favorable for a weak Antarctic stratospheric polar vortex. Rao et al. (2019b) reported that the January 2019 NH SSW also occurred under several favorable conditions: the easterly QBO at 50 hPa, the solar minimum, moderate El Niño, and MJO phases 4–6. The average predictive limit in S2S models for the January 2019 NH SSW is also ~18 days. The low-top S2S models (BOM, CMA-BCC, ECCC, HMCR, and ISAC-CNR) usually have reduced skill in predicting SSW events due to their lack of a well-resolved stratosphere (e.g., Rao et al., 2019a, 2020; Domeisen et al., 2020a, 2020b). These low-top models also failed to predict the September 2019 SH SSW event, as is evident from their relatively low hit ratio.

There are four common initializations within one month before the real SSW onset for all S2S model except JMA—22 August, 29 August, 5 September, and 12 September—while forecasts initialized one day earlier are available for JMA. The predicted evolutions of $[U]_{10\text{hPa}/60\text{S}}$ in the four initializations (color) for all S2S models are shown in Figure 7, with JMA initializations shown from one day earlier. Zonal winds at 10 hPa are not provided by HMCR, so the evolution of zonal winds at 50 hPa is shown for this model. The ECCC model fails to properly initialize the SH stratosphere in the lead-up to the September 2019 SSW (Figure 7c), although the model has a reasonable initialization in the NH stratosphere during

the February 2018 and January 2019 NH SSWs (Rao et al., 2019b, 2020). Deceleration of the westerly winds at 50 hPa is much smaller than the winds at 10 hPa, and the HMCR (Figure 7e) shows a large prediction spread for the westerly wind around 16 September especially in the two early forecast ensembles (in purple and green). Other models can well predict the strong deceleration of the circumpolar winds before 16 September even in the two earlier forecast ensembles, although most ensemble members in some models (e.g., BOM, ECCC, ISAC-CNR, JMA) fail to forecast the weak westerlies that decelerated to <20 m/s around 16 September, consistent with the small hit ratio for those initializations in low-top models in Figure 6. In the 29 August initialization, some models (ECMWF, JMA, KMA, NCEP, UKMO) successfully predict the deceleration of the westerlies to <20 m/s (Figures 7d, 7g, 7h, 7j, 7k). These five models have a high model top and a well-resolved stratosphere, which is consistent with previous work that indicates an improved representation of the stratosphere adds some skill to the SSW prediction (Roff et al., 2011; Son et al., 2013; Rao et al., 2019b).

5.2 Prediction of the persistent tropospheric circulation pattern

The wave-1 forcing that displaces the SH stratospheric polar vortex toward the Antarctic Peninsula (Figure 3c) can be tracked to the troposphere. The tropospheric circumglobal wave train-like anomaly pattern has been shown in Section 4 to be likely associated with the positive IOD and moderate warm SST anomalies in the central Pacific. The prediction of the SH extratropical height anomalies at 500 hPa is shown in Figure 8 for the multi-model ensemble mean (MME) initialized on 22 August, 29 August, 5 September, and 12 September, respectively. Based on the reanalysis, the height anomaly centers (especially the high blocking over the Antarctic Peninsula and the anomalous low center over the South Indian Ocean) show a long lifetime in different sub-periods before and during the SSW (shadings in Figure 8). The earliest initialization on 22 August well forecasts the extratropical height pattern during 31 August–4 September (Figure 8a; PCC = 0.8), including the Antarctic Peninsula anomaly high and the South Indian Ocean anomaly low. The tropospheric predictive skill in the 22 August initialization MME decreases rapidly in the following three sub-periods (Figures 8b–8d; PCC < 0.5). The predictive skill for this SSW onset in the 22 August initialization might also originate from stratospheric predictability (i.e., QBO and solar cycle).

The MME initialized on 29 August can reasonably forecast the tropospheric height patterns in all of the four successive sub-periods (Figures 8e–8h; PCC > 0.5), although the magnitude of the eddy height anomalies is largely underestimated during 5–9, 14–10, and 15–19 September (e.g., the high center: ~160 vs 60 gpm). The amplitude of the predicted wave pattern also decreases with the forecast time for the 5 September initialization (Figures 8i–8k; PCC ≥ 0.5), consistent with the high hit ratio in most models for this initialization (Figure 6). Since the initialization time is much closer to the SSW onset date in the 12 September initialization MME, the amplitude and phase of the eddy height during 15–19 September are forecasted correctly (Figure 8l; PCC = 0.91). The MMEs for some high-top models (ECMWF, KMA, JMA, NCEP, and ECMWF) and the remaining models are also compared. The pattern correlation for high-top models are very similar to low-top models, but the height anomaly

magnitude in the high-top MME is better predicted than in the low-top MME (not shown for succinctness).

5.3 Prediction of the wave forcing in forecasts

To test the contribution of the upward propagation of waves to the SSW predicative skill, the scatter plot of the cumulative eddy heat flux by wave-1 ($\propto -F_z$ in the SH) averaged in the 45–75°S latitude band at 500 hPa from 7–16 September (i.e., within ten days before the SSW onset) versus the zonal mean winds at 60°S and 10 hPa (50 hPa for HMCR) during 16–20 September is shown in Figure 9a. Only the ensemble mean for the common initializations and each model is shown. Note that negative eddy heat flux corresponds to upward EP flux in the SH, while positive eddy heat flux in the SH denotes weak wave activity from the troposphere to the stratosphere. For the two earlier initializations, nearly all forecasting models tend to underestimate the upward propagation of waves, explaining the much stronger westerlies in forecasts (purple and green in Figure 9a). The zonal mean zonal wind in HMCR seems to be outliers, because the wind at 50 hPa is shown for this model due to the unavailability of the zonal wind at 10 hPa. The forecasted cumulative eddy heat flux and zonal winds in the 29 August initialization by ECMWF, JMA, KMA, and UKMO (#4, #7, #8, #11 in green) are closer to observations than that forecasted by other models. In contrast, the upward propagation of waves and the zonal mean zonal winds are forecasted by most models in the 5 September initializations (orange in Figure 9a), consistent with the high tropospheric predictive skill in the MME (Figures 8i–8k). For the 12 September initialization (red in Figure 9a), the reanalysis is used to complete the 10-day cumulative eddy heat flux (7–16 September), and the bias relative to observations is fairly small, mainly reflecting the bias in the last five days (12–16 September). The correlation between the cumulative eddy heat flux bias (relative to observations) and the zonal mean zonal wind bias (relative to observations) is 0.38, indicating the importance of the tropospheric forcing for the SSW event and its predictability. The relationship between the cumulative heat flux bias by wave-1 at 100 hPa and the zonal mean zonal wind bias at 10 hPa is also calculated (Figure 9b), and their correlation (0.85) becomes much larger than in Figure 9a at a higher confidence level ($\alpha \approx 0.0$).

5.4 Impact of the September 2019 SSW on the near surface predictability

The prediction of the near surface temperature and precipitation anomalies in the 15 days following the SSW onset (i.e., 16–30 September) is shown in Figure 10 for two initializations. In observations, Australia was anomalously warm in late September 2019 (Figure 10e), and southeast Australia was dry (Figure 10j). Such a warm and dry Australian pattern is often associated with a positive IOD and warm SST anomalies in central Pacific (Lim et al., 2019; Figure 4b). The stratospheric anomalies during the SSW appears to have had little immediate impact on the troposphere, and no SAM-like signal propagated downward to the troposphere in the following 15 days (shadings in Figures 10a, 10c). However, the MME forecasts show stronger easterly anomalies in the lower stratosphere than the reanalysis for the two initializations (contours in Figures 10a, 10c). In other words, a more negative tropospheric SAM is forecasted in MME, though not observed (Figures 10b, 10d).

The warm Australia during 16–30 September is well forecasted in the 29 August and 5 September initialization MMEs, and the PCC between the observation and forecasts for the 2-m temperature is 0.64 and 0.68 (Figures 10f, 10i). We do not associate the Australian warm conditions in late September to the stratospheric event, because no negative SAM can be tracked to the SSW in the observation (Figures 2c, 2i). In this case, it is suggested that the predictability of the 2-m temperature on the S2S timescale can likely be attributed to the SST forcing in the neighboring oceans. However, part of Australia was predicted to be warmer than observed (Figures 10g, 10i), likely due to a spurious negative tropospheric SAM resulting from a stronger and faster downward propagation of the SSW in forecasts (Figures 10b, 10d).

The land precipitation is less predictable than the 2-m temperature in the SH, as in the NH (Karpenko et al., 2018; Rao et al., 2020). The dry conditions in the south and east parts of Australia, reminiscent of the rainfall pattern during positive IOD (http://www.bom.gov.au/climate/iod/), is largely underestimated in S2S models (Figures 10k, 10m): there is no forecast skill in the 29 August initialization (PCC = -0.06) and low skill in the 5 September initialization (PCC = 0.27). The predicted rainfall bias is largest in southeast Australia (Figures 10l, 10n), which can also be partially attributed to the forecasted tropospheric SAM bias associate with a faster downward propagation of the SSW in forecasts (Figures 10b, 10d). The negative tropospheric SAM was observed in October and November 2019 and the downward propagation of negative SAM appeared much later, well after the SSW onset (not shown). The SAM affected Australian climate by inducing changes in surface temperatures and rainfall across southern and eastern parts of the continent (Gillett et al., 2006; Hendon et al., 2007; Min et al., 2013; Lim & Hendon, 2015; Lim et al., 2019). Due to the limited forecast duration of the S2S models, the prediction of surface impacts in October and November 2019 (i.e. far beyond the SSW onset day) is not discussed.

6 Summary and discussion

There have only been two recorded SH SSWs: one in September 2002 when the circumpolar westerlies reversed to easterlies, and the other in September 2019 without a zonal wind reversal at 60°S and 10 hPa. Even though the circumpolar westerlies at 60°S did not reverse in September 2019, the westerlies at 50°S did indeed reverse and the observed Antarctic polar cap height and temperature anomalies during the September 2019 SSW are comparable to the September 2002 SSW. The September 2002 SSW has been widely reported in literature, but the September 2019 event and its predictability have not been yet. Using the real-time multivariate MJO daily time series, the COBE SST dataset, the QBO observations, the solar flux at 10.7cm, the reanalysis dataset, and real-time forecasts from 11 S2S forecasting models, several aspects of the September 2019 SH SSW are analyzed, including the observed evolution of this SSW, the favorable conditions for the tropospheric and stratosphere circulation patterns during this SSW, and the predictability of this SSW. The main findings are as follows.

i. The deceleration of $[U]_{10\text{hPa/60S}}$ and the wind anomalies for the September 2019 SH SSW are even larger than some NH SSWs. This might imply that the cumulative wave flux needed for a SH SSW is much larger than an average SSW event in the NH, because the climatological SH night jet is much stronger than the NH counterpart (>80 m/s vs

492 ~30 m/s at 10hPa). Using a strict definition of SSW as in the NH, the September 2019
493 SSW would not be identified as a major SSW. We adopt here a less strict definition to
494 identify a SH SSW (e.g., threshold: 20 m/s for $[U]_{10hPa/60S}$ vs 0 m/s for $[U]_{10hPa/60N}$),
495 though the zero wind definition applied at 50°S would also classify this SSW as major.
496 ii. Similar to some NH SSWs occurring under favorable conditions, the September 2019
497 SSW happened during the easterly QBO10, the solar minimum, the positive IOD,
498 moderate warm SST anomalies in the central Pacific, and the extratropical blocking
499 over Antarctic Peninsula. The MJO amplitude before the SSW onset is weak, and
500 contribution by the MJO-related convection anomalies to the weakening of the polar
501 vortex is unlikely. Local warm SST anomalies over the western tropical Indian Ocean
502 and central Pacific led to locally enhanced tropical convection. The composite analysis
503 shows that easterly QBO10 excites a high anomaly center over South Indian Ocean at
504 10 hPa, and the solar minimum induces a low anomaly center over South Atlantic
505 Ocean, both of which are nearly in phase with the observed wave-1-like pattern in
506 September 2019. Composites of the positive IOD and warm SST in the central Pacific
507 corresponds to a circumpolar wave train-like circulation pattern at 500 hPa, highly
508 resembling the observed anomaly pattern in September 2019. Namely, a ridge
509 developed in the subpolar Southeast Pacific, which constructively interfered with the
510 climatological planetary waves.
511 iii. With those favorable initial and boundary conditions for S2S models, the predictive
512 limit to the September 2019 SH SSW is >18 days in the high-top forecasting models.
513 The SSW hit ratio in a common early initialization around 29 August even exceeds 50%
514 in those models with a decently-resolved stratosphere. The zonal-mean westerlies in
515 this initialization and in later ones evolve essentially as in observations.
516 iv. The long-lived tropospheric precursors (e.g., the high anomaly center associated with
517 blocking over the Antarctic Peninsula, and the low anomaly center over the South
518 Indian Ocean) before this SSW are forecasted to different degrees of success during
519 four focused sub-periods. The early initialization MME around 22 August has a low
520 predictive skill for the tropospheric anomaly pattern a few days before the SSW onset
521 (PCC < 0.5). The initializations later than 29 August capture the wave-like pattern in
522 the MME, although the wave amplitude is underestimated.
523 v. Inter-forecast spread in the westerly winds during the SSW onset is correlated with the
524 inter-forecast spread in the cumulative upward propagation of waves from the
525 troposphere to the stratosphere. The weaker-than-observed upward E-P flux in models
526 for early initializations results from the underestimated wave magnitude in the
527 troposphere, and in turn leads to a too-weak weakening of the vortex.
528 vi. The September 2019 SH SSW did not show an instant downward impact on the
529 tropospheric SAM after its onset in late September and early October 2019. Therefore,
530 the Australian drought and hot weather possibly initialized by the positive IOD in
531 September 2019 may have been exacerbated by the negative SAM in late October and
532 following months associated with the preexisting weak stratospheric polar vortex (Lim
533 et al., 2019). However, the MME forecasts a stronger stratosphere-troposphere coupling

and an instant impact of the SSW on the near surface weather.

The long lead-time predictability of the September 2019 SH SSW is reminiscent of the similarly long-leads at which the January 2019 NH SSW was predicted: both were forecasted at lead times of ~20 days. The January 2019 NH SSW was also preceded by favorable initial and boundary conditions: the easterly QBO at 50 hPa, the solar minimum, moderate El Niño, and MJO phases 4–6 (Rao et al., 2019b, 2020). Similar to the January 2019 NH event, the September 2019 SH event is also a vortex displacement event, which has been shown to be better forecasted (on average) than a vortex split SSW (Rao et al., 2019a, 2019b; Taguchi, 2018, 2020). Although the predictability of SSWs in the NH has recently been reported widely (Karpechko, 2018; Karpechko et al., 2018; Taguchi, 2018, 2020; Rao et al., 2019a, 2019b, 2020; Domeisen et al., 2020a, 2020b), this study enriches literature about the predictability of SSWs in the SH. Our results also further confirm that the predictive skill of forecasting models for some SSWs can exceed two weeks if the initial and boundary conditions are favorable for occurrence of a weak stratospheric polar vortex.

Acknowledgements

JR acknowledges the National Natural Science Foundation of China (41705024) and the National Key R&D Program of China (2016YFA0602104). This research was also supported by the ISF-NSFC joint research program (3259/19), and the European Research Council starting grant under the European Unions Horizon 2020 research and innovation programme (677756). The authors also acknowledge the 11 S2S model agencies and NCAR/NCEP for providing the S2S real-time predictions (https://apps.ecmwf.int/datasets/data/s2s/levtype=sfc/type=cf/) and reanalysis (https://www.esrl.noaa.gov/psd/data/gridded/data.ncep.reanalysis. html) data, respectively.

References

Allen, D. R., Bevilacqua, R. M., Nedoluha, G. E., Randall, C. E., & Manney, G. L. (2003). Unusual stratospheric transport and mixing during the 2002 Antarctic winter. *Geophysical Research Letters*, *30*, 1599. https://doi.org/10.1029/2003gl017117

Allen, D. R., Coy, L., Eckermann, S. D., McCormack, J. P., Manney, G. L., Hogan, T. F., & Kim, Y. J. (2006). NOGAPS-ALPHA simulations of the 2002 Southern Hemisphere stratospheric major warming. *Monthly Weather Review*, *134*, 498–518. https://doi.org/10.1175/mwr3086.1

Arblaster, J. M., & Meehl, G. A. (2006). Contributions of External Forcings to Southern Annular Mode Trends. *Journal of Climate*, *19,* 2896–2905.

Baldwin, M. P., & Dunkerton, T. J. (1998). Quasi-biennial modulation of the southern hemisphere stratospheric polar vortex. *Geophysical Research Letters*, *25*, 3343–3346. https://doi.org/10.1029/98gl02445

Baldwin, M. P., & Dunkerton, T. J. (1999). Propagation of the Arctic Oscillation from the stratosphere to the troposphere. *Journal of Geophysical Research: Atmospheres*, *104*, 30937–30946. https://doi.org/10.1029/1999jd900445

Baldwin, M. P., & Dunkerton, T. J. (2001). Stratospheric harbingers of anomalous weather

574 regimes. *Science*, *294*, 581–584. https://doi.org/10.1126/science.1063315
575 Baldwin, M. P., Stephenson, D. B., Thompson, D. W. J., Dunkerton, T. J., Charlton, A. J., &
576 O'Neill, A. (2003). Stratospheric memory and skill of extended-range weather forecasts.
577 *Science*, *301*, 636–640. https://doi.org/10.1126/science.1087143
578 Butler, A. H., Seidel, D. J., Hardiman, S. C., Butchart, N., Birner, T., & Match, A. (2015).
579 Defining sudden stratospheric warmings. *Bulletin of the American Meteorological Society,*
580 *96*, 1913–1928. https://doi.org/10.1175/bams-d-13-00173.1
581 Butler, A. H., & Gerber, E. P. (2018). Optimizing the definition of a sudden stratospheric
582 warming. *Journal of Climate*, *31*, 2337–2344. https://doi.org/10.1175/jcli-d-17-0648.1
583 Byrne, N. J., & Shepherd, T. G. (2018). Seasonal persistence of circulation anomalies in the
584 Southern Hemisphere stratosphere and its implications for the troposphere. *Journal of*
585 *Climate*, *31*, 3467–3483. https://doi.org/10.1175/jcli-d-17-0557.1
586 Charlton, A. J., O'Neill, A., Stephenson, D. B., Lahoz, W. A., & Baldwin, M. P. (2003). Can
587 knowledge of the state of the stratosphere be used to improve statistical forecasts of the
588 troposphere? *Quarterly Journal of the Royal Meteorological Society*, *129*, 3205–3224.
589 https://doi.org/10.1256/qj.02.232
590 Charlton, A. J., & Polvani, L. M. (2007). A new look at stratospheric sudden warmings. Part I:
591 Climatology and modeling benchmarks. *Journal of Climate, 20*, 449–469.
592 https://doi.org/10.1175/jcli3996.1
593 Chen, Dan, Strube, C., Ern, M., Preusse, P., & Riese, M. (2019). Global analysis for periodic
594 variations in gravity wave squared amplitudes and momentum fluxes in the middle
595 atmosphere. *Annales Geophysicae*, 2019, *37*, 487–506. https://doi.org/ 10.5194/angeo-37-
596 487-2019
597 Domeisen, D. I. V., Butler, A. H., Charlton-Perez, A. J., Ayarzagüena, B., Baldwin, M. P.,
598 Dunn-Sigouin, E., et al. (2020a). The role of the stratosphere in subseasonal to seasonal
599 prediction: 1. Predictability of the stratosphere. *Journal of Geophysical Research:*
600 *Atmospheres*, *125,* e2019jd030920. https://doi.org/10.1029/2019jd030920
601 Domeisen, D. I. V., Butler, A. H., Charlton-Perez, A. J., Ayarzagüena, B., Baldwin, M. P.,
602 Dunn-Sigouin, E., et al. (2020b). The role of the stratosphere in subseasonal to seasonal
603 prediction: 2. Predictability arising from stratosphere - troposphere coupling. *Journal of*
604 *Geophysical Research: Atmospheres*, *125*, e2019jd030923,
605 https://doi.org/10.1029/2019jd030923
606 Garfinkel, C. I., & Schwartz, C. (2017). MJO-related tropical convection anomalies lead to
607 more accurate stratospheric vortex variability in subseasonal forecast models. *Geophysical*
608 *Research Letters*, *44*, 10054–10062, https://doi.org/10.1002/2017gl074470
609 Garfinkel, C. I., Waugh, D. W., & Gerber, E. P., (2013). The effect of tropospheric jet latitude
610 on coupling between the stratospheric polar vortex and the troposphere. *Journal of Climate*,
611 *26*, 2077–2095. https://doi.org/ 10.1175/jcli-d-12-00301.1
612 Gerber, E. P., Orbe, C., & Polvani, L. M. (2009). Stratospheric influence on the tropospheric
613 circulation revealed by idealized ensemble forecasts. *Geophysical Research Letters*, *36*,
614 L24801. https://doi.org/10.1029/2009gl040913
615 Gerber, E. P., Butler, A., Calvo, N., Charlton-Perez, A., Giorgetta, M., Manzini, E, et al. (2012).

Assessing and understanding the impact of stratospheric dynamics and variability on the earth system. *Bulletin of the American Meteorological Society, 93,* 845–859. https://doi.org/10.1175/bams-d-11-00145.1

Gillett, N. P., Kell, T. D., & Jones, P. D. (2006). Regional climate impacts of the Southern Annular Mode. *Geophysical Research Letters*, *33,* L23704. https://doi.org/10.1029/2006gl027721

Gillett, N. P., & Thompson, D. W. (2003). Simulation of recent Southern Hemisphere climate change. *Science*, *302*, 273–275. https://doi.org/10.1126/science.1087440

Hendon, H. H., Thompson, D. W. J., & Wheeler, M. C. (2007). Australian rainfall and surface temperature variations associated with the Southern Hemisphere annular mode. *Journal of Climate*, *20*, 2452–2467. https://doi.org/10.1175/jcli4134.1

Hio, Y., & Yoden, S. (2005). Interannual variations of the seasonal march in the Southern Hemisphere stratosphere for 1979–2002 and characterization of the unprecedented year 2002. *Journal of the Atmospheric Sciences, 62*, 567–580. https://doi.org/10.1175/jas-3333.1

Hitchcock, P., & Shepherd, T. G. (2013). Zonal-mean dynamics of extended recoveries from stratospheric sudden warmings. *Journal of the Atmospheric Sciences, 70*, 688–707. https://doi.org/10.1175/jas-d-12-0111.1

Hitchcock, P., & Simpson, I. R. (2014). The downward influence of stratospheric sudden warmings. *Journal of the Atmospheric Sciences, 71*, 3856–3876. https://doi.org/10.1175/jas-d-14-0012.1

Hurwitz, M., Newman, P., Oman, L., & Molod, A. (2011). Response of the Antarctic stratosphere to two types of El Niño events. *Journal of the Atmospheric Sciences, 68*, 812–822.

Kalnay, E., Kanamitsu, M., Kistler, R., Collins, W., Deaven, D., Gandin, L., et al. (1996). The NCEP/NCAR 40-year reanalysis project. *Bulletin of the American Meteorological Society*, *77*, 437–471.

Karpechko, A. Y. (2018). Predictability of sudden stratospheric warmings in the ECMWF extended-range forecast system. *Monthly Weather Review*, *146*, 1063–1075. https://doi.org/10.1175/mwr-d-17-0317.1

Karpechko, A. Y., Charlton-Perez, A., Balmaseda, M., Tyrrell, N., & Vitart, F. (2018). Predicting sudden stratospheric warming 2018 and its climate impacts with a multimodel ensemble. *Geophysical Research Letters*, *45*, 13538–13546. https://doi.org/10.1029/2018gl081091

Kidston, J., Scaife, A. A., Hardiman, S. C., Mitchell, D. M., Butchart, N., Baldwin, M. P., & Gray, L. J. (2015). Stratospheric influence on tropospheric jet streams, storm tracks and surface weather. *Nature Geoscience*, *8*, 433–440. https://doi.org/10.1038/ngeo2424

Kistler, R., Kalnay, E., Collins, W., Saha, S., White, G., Woollen, J., et al. (2001). The NCEP-NCAR 50-year reanalysis: Monthly means CD-ROM and documentation. *Bulletin of the American Meteorological Society*, *82*, 247–267.

Kobayashi, S., Ota, Y., Harada, Y., Ebita, A., Moriya, M., Onoda, H., et al. (2015). The JRA-55 reanalysis: General specifications and basic characteristics. *Journal of the*

Meteorological Society of Japan, 93, 5–48. https://doi.org/10.2151/jmsj.2015-001

Kodera, K., & Kuroda, Y. (2002). Dynamical response to the solar cycle. *Journal of Geophysical Research: Atmospheres*, *107*, 4749. https://doi.org/10.1029/2002jd002224

Kuroda, Y., & Kodera, K. (1998). Interannual variability in the troposphere and stratosphere of the southern hemisphere winter. *Journal of Geophysical Research: Atmospheres*, *103*, 13787–13799. https://doi.org/10.1029/98jd01042

Kuroda, Y., & Kodera, K. (2005). Solar cycle modulation of the southern annular mode. *Geophysical Research Letters, 32*, L13802. https://doi.org/10.1029/2005gl022516

Lahoz, W. A. (1999). Predictive skill of the UKMO unified model in the lower stratosphere. *Quarterly Journal of the Royal Meteorological Society, 125*, 2205–2238. https://doi.org/10.1002/qj.49712555813

Lim, E.-P., & Hendon, H. H. (2015). Understanding the contrast of Australian springtime rainfall of 1997 and 2002 in the frame of two flavors of El Niño. *Journal of Climate*, *28,* 2804–2822. https://doi.org/10.1175/jcli-d-14-00582.1

Lim, E.-P., Hendon, H. H., Boschat, G., Hudson, D., Thompson, D. W. J., Dowdy, A. J., & Arblaster, J. M. (2019). Australian hot and dry extremes induced by weakenings of the stratospheric polar vortex. *Nature Geoscience*, *12*, 896–901. https://doi.org/10.1038/s41561-019-0456-x

Lim, E. P., Hendon, H. H., & Thompson, D. W. J. (2018). Seasonal evolution of stratosphere-troposphere coupling in the southern hemisphere and implications for the predictability of surface climate. *Journal of Geophysical Research: Atmospheres*, *123*, 12002–12016. https://doi.org/10.1029/2018jd0293

Min, S.-K., Cai, W., & Whetton, P. (2013). Influence of climate variability on seasonal extremes over Australia. *Journal of Geophysical Research: Atmospheres*, *118,* 643–654. https://doi.org/10.1002/jgrd.50164

Naito, Y. (2002). Planetary wave diagnostics on the QBO effects on the deceleration of the polar-night jet in the Southern Hemisphere. *Journal of the Meteorological Society of Japan*, *80*, 985–995. https://doi.org/10.2151/jmsj.80.985

Polvani, L. M., Waugh, D. W., Correa, G. J. P., & Son, S.-W. (2011). Stratospheric ozone depletion: The main driver of twentieth-century atmospheric circulation changes in the Southern Hemisphere. *Journal of Climate*, *24*, 795–812. https://doi.org/10.1175/2010jcli3772.1

Randel, W. J. (1988). The seasonal evolution of planetary waves in the southern hemisphere stratosphere and troposphere. *Quarterly Journal of the Royal Meteorological Society*, *114*, 1385–1409. https://doi.org/10.1002/qj.49711448403

Rao, J., Ren, R. Chen, H., Yu, Y., & Zhou Y. (2018). The stratospheric sudden warming event in February 2018 and its prediction by a climate system model. *Journal of Geophysical Research: Atmospheres*, *123*, 13332–13345. https://doi.org/ 10.1029/2018jd028908

Rao, J., Ren, R., Chen, H., Liu, X., Yu, Y., Hu, J. & Zhou, Y. (2019a). Predictability of stratospheric sudden warmings in the Beijing Climate Center forecast system with statistical error corrections. *Journal of Geophysical Research: Atmospheres*, *124*, 8385–8400. https://doi.org/ 10.1029/2019JD030900

700 Rao, J., Garfinkel, C. I., Chen, H., & White, I. P. (2019b). The 2019 New Year stratospheric
701 sudden warming and its real-time predictions in multiple S2S models. *Journal of*
702 *Geophysical Research: Atmospheres*, *124*, 11155–11174. https://doi.org/
703 10.1029/2019jd030826
704 Rao, J., Garfinkel, C. I., & White, I. P. (2020). Predicting the downward and surface influence
705 of the February 2018 and January 2019 sudden stratospheric warming events in
706 subseasonal to seasonal (S2S) models. *Journal of Geophysical Research: Atmospheres*,
707 *125*, e2019JD031919. https://doi.org/10.1029/2019jd031919
708 Rao, J., & Ren, R. (2020). Modeling study of the destructive interference between tropical
709 Indian Ocean and Eastern Pacific in their forcing in the southern winter extratropical
710 stratosphere during ENSO. *Climate Dynamics, 54*, 2249–2266.
711 https://doi.org/10.1007/s00382-019-05111-6
712 Ren, R., & Cai, M. (2008). Meridional and downward propagation of atmospheric circulation
713 anomalies. Part II: Southern Hemisphere cold season variability. *Journal of the*
714 *Atmospheric Sciences, 65*, 2343–2359. https://doi.org/10.1175/2007jas2594.1
715 Roff, G., Thompson, D. W. J., & Hendon, H. (2011). Does increasing model stratospheric
716 resolution improve extended-range forecast skill? *Geophysical Research Letters*, *38*,
717 L05809. https://doi.org/10.1029/2010gl046515
718 Simmons, A., Hortal, M., Kelly, G., McNally, A., Untch, A., & Uppala, S. (2005). ECMWF
719 analyses and forecasts of stratospheric winter polar vortex breakup: September 2002 in the
720 Southern Hemisphere and related events. *Journal of the Atmospheric Sciences, 62*, 668–
721 689. https://doi.org/10.1175/jas-3322.1
722 Sigmond, M., Scinocca, J. F., Kharin, V. V., & Shepherd, T. G. (2013). Enhanced seasonal
723 forecast skill following stratospheric sudden warmings. *Nature Geoscience*, *6*, 98–102.
724 https://doi.org/10.1038/ngeo1698
725 Son, S. W., Gerber, E. P., Perlwitz, J., Polvani, L. M., Gillett, N. P., Seo, K. H., et al. (2010).
726 Impact of stratospheric ozone on Southern Hemisphere circulation change: A multimodel
727 assessment. *Journal of Geophysical Research: Atmospheres*, *115*, D00M07.
728 https://doi.org/10.1029/2010jd014271
729 Son, S.-W., Purich, A., Hendon, H. H., Kim, B.-M., & Polvani, L. M. (2013). Improved
730 seasonal forecast using ozone hole variability? *Geophysical Research Letters*, *40*, 6231–
731 6235. https://doi.org/10.1002/2013gl057731
732 Taguchi, M. (2018). Comparison of subseasonal-to-seasonal model forecasts for major
733 stratospheric sudden warmings. *Journal of Geophysical Research: Atmospheres*, *123*,
734 10231–10247. https://doi.org/10.1029/2018jd028755
735 Taguchi, M. (2020). Verification of subseasonal-to-seasonal forecasts for major stratospheric
736 sudden warmings in northern winter from 1998/99 to 2012/13. *Advances in Atmospheric*
737 *Sciences*, *37*, 250–258. https://doi.org/10.1007/s00376-019-9195-6
738 Thompson, D. W. J., Baldwin, M. P., & Solomon, S. (2005). Stratosphere–troposphere coupling
739 in the Southern Hemisphere. *Journal of the Atmospheric Sciences, 62*, 608–715.
740 https://doi.org/10.1175/jas-3321.1
741 Tripathi, O. P., Baldwin, M., Charlton-Perez, A., Charron, M., Eckermann, S. D., Gerber, E.,

et al. (2015). The predictability of the extratropical stratosphere on monthly time-scales and its impact on the skill of tropospheric forecasts. *Quarterly Journal of the Royal Meteorological Society*, *141*, 987–1003. https://doi.org/10.1002/qj.2432

Tripathi, O. P., Baldwin, M., Charlton-Perez, A., Charron, M., Cheung, J. C. H., Eckermann, S. D., et al. (2016). Examining the predictability of the stratospheric sudden warming of january 2013 using multiple NWP systems. *Monthly Weather Review, 144,* 1935–1960. https://doi.org/10.1175/mwr-d-15-0010.1

Vitart, F. (2014). Evolution of ECMWF sub-seasonal forecast skill scores. *Quarterly Journal of the Royal Meteorological Society*, *140*, 1889–1899. https://doi.org/10.1002/qj.2256

Waugh, D. W., Garfinkel, C. I., & Polvani, L. M. (2015). Drivers of the recent tropical Expansion in the Southern Hemisphere: Changing SSTs or ozone depletion? *Journal of Climate*, *28***,** 6581–6586. https://doi.org/10.1175/jcli-d-15-0138.1

Waugh, D. W., Sisson, J. M., & Karoly, D. J. (1998). Predictive skill of an NWP system in the southern lower stratosphere. *Quarterly Journal of the Royal Meteorological Society*, *124*, 2181–2200. https://doi.org/10.1002/qj.49712455102

Waugh, D. W., Sobel, A. H., & Polvani, L. M. (2017). What is the polar vortex and how does it influence weather? *Bulletin of the American Meteorological Society, 98*, 37–44. https://doi.org/10.1175/bams-d-15-00212.1

Wheeler, M. C., & Hendon, H. H. (2004). An all-season real-time multivariate MJO index: Development of an index for monitoring and prediction. *Monthly Weather Review, 132*, 1917–1932.

White, I., Garfinkel, C. I., Gerber, E. P., Jucker, M., Aquila, V., & Oman, L. D. (2019). The downward influence of sudden stratospheric warmings: Association with tropospheric precursors. *Journal of Climate, 32*, 85–108. https://doi.org/ 10.1175/jcli-d-18-0053.1

Woollings, T., Charlton-Perez, A., Ineson, S., Marshall, A. G., & Masato, G. (2010). Associations between stratospheric variability and tropospheric blocking. *Journal of Geophysical Research: Atmospheres*, *115*, D06108. https://doi.org/10.1029/2009jd012742

Yamazaki, Y., Matthias, V., Miyoshi, Y., Stolle, C., Siddiqui, T., Kervalishvili, G., et al. (2020). September 2019 Antarctic sudden stratospheric warming: Quasi-6-day wave burst and ionospheric effects. *Geophysical Research Letters*, *47*, e2019GL086577. https://doi.org/10.1029/2019gl086577

Yang, C., Li, T., Smith, A. K., & Dou, X. (2017). The response of the Southern Hemisphere middle atmosphere to the Madden–Julian Oscillation during austral winter using the Specified-Dynamics Whole Atmosphere Community Climate Model. *Journal of Climate*, *30***,** 8317–8333. https://doi.org/10.1175/jcli-d-17-0063.1

Zubiaurre, I., & Calvo, N. (2012). The El Niño–Southern Oscillation (ENSO) Modoki signal in the stratosphere. *Journal of Geophysical Research: Atmospheres, 117*, D04104. https://doi.org/10.1029/2011jd016690

Figures and captions

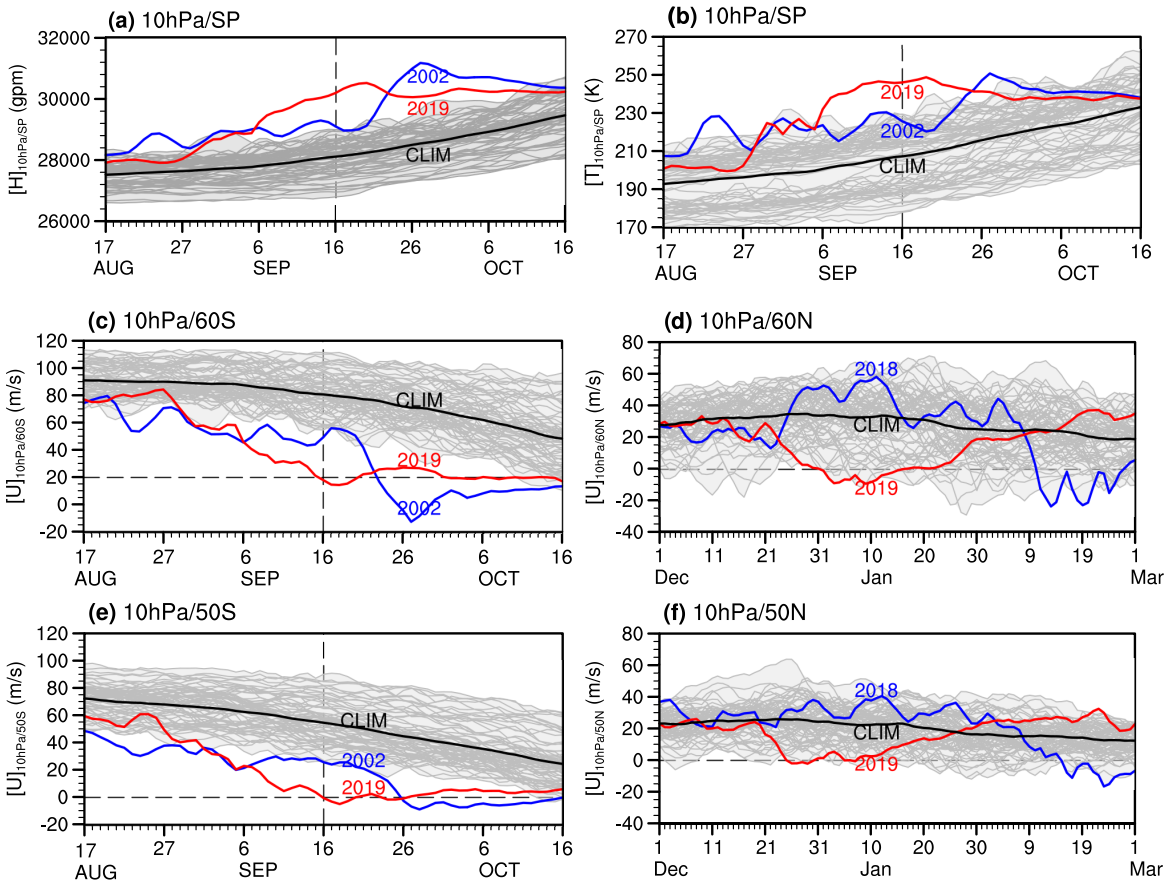

Figure 1. (a) Day-by-day evolutions of the area-mean geopotential height in the Antarctic stratosphere (poleward of 65°S) at 10 hPa from 17 August to 16 October for each year (1948–2019). The dark gray curves are the years without SSW events, and the light shading mark the value ranges in those years. The two SSW events in 2002 and 2019 are highlighted in colors. The black curve is the climatology. (b) As in (a) but for the area-mean temperature at 10 hPa. (c) As in (a), but for the zonal-mean zonal wind at 10 hPa and 60°S. (d) Day-by-day evolutions of the zonal-mean zonal wind at 10 hPa and 60°N from 1 December to 1 March for each northern winter (1948/49–2018/19). The two most recent SSWs (February 2018 and January 2019) in the Northern Hemisphere are also highlighted in colors. (e, f) As in (c, d) but for the zonal-mean zonal winds at 10 hPa and 50°S/N.

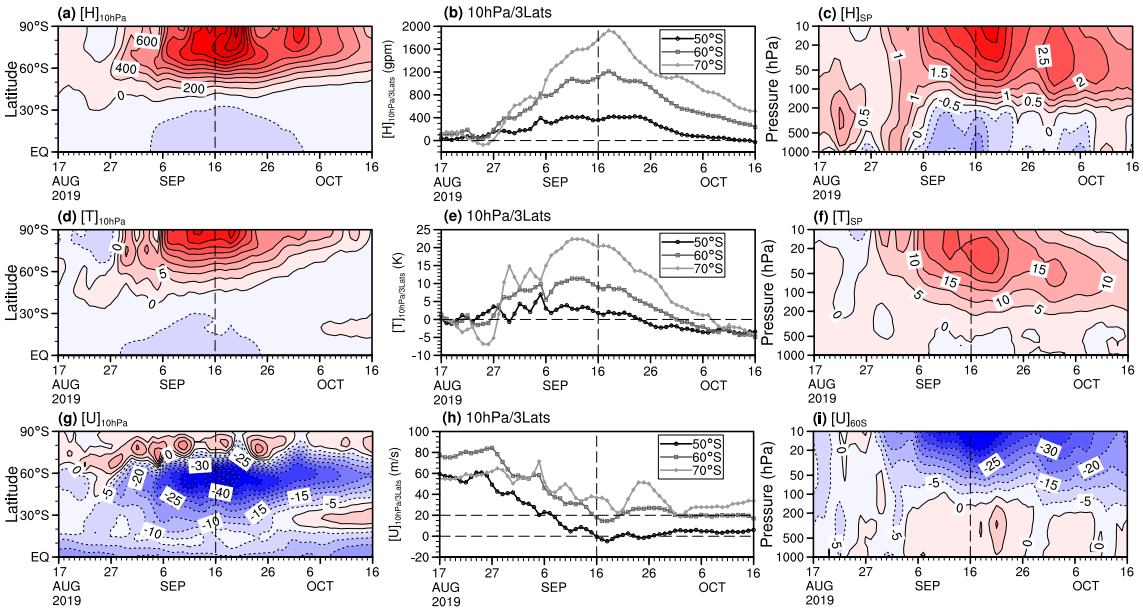

Figure 2. (a) Latitude-temporal evolution of the zonal-mean geopotential height anomalies (units: gpm) at 10 hPa from 17 August to 16 October 2019. (b) Evolution of the zonal-mean geopotential height anomalies at 10 hPa for three latitudes. (c) Pressure-time evolution of the normalized Antarctic geopotential height anomalies. (d–f) As in (a–c), but for the zonal-mean temperature. (g–i) As in (a–c), but the zonal-mean zonal wind. Note that the Antarctic height anomalies in Figure 2c have been normalized by the daily deviation at each pressure level to enhance visualization. The full zonal-mean zonal winds are shown in Figure 2h.

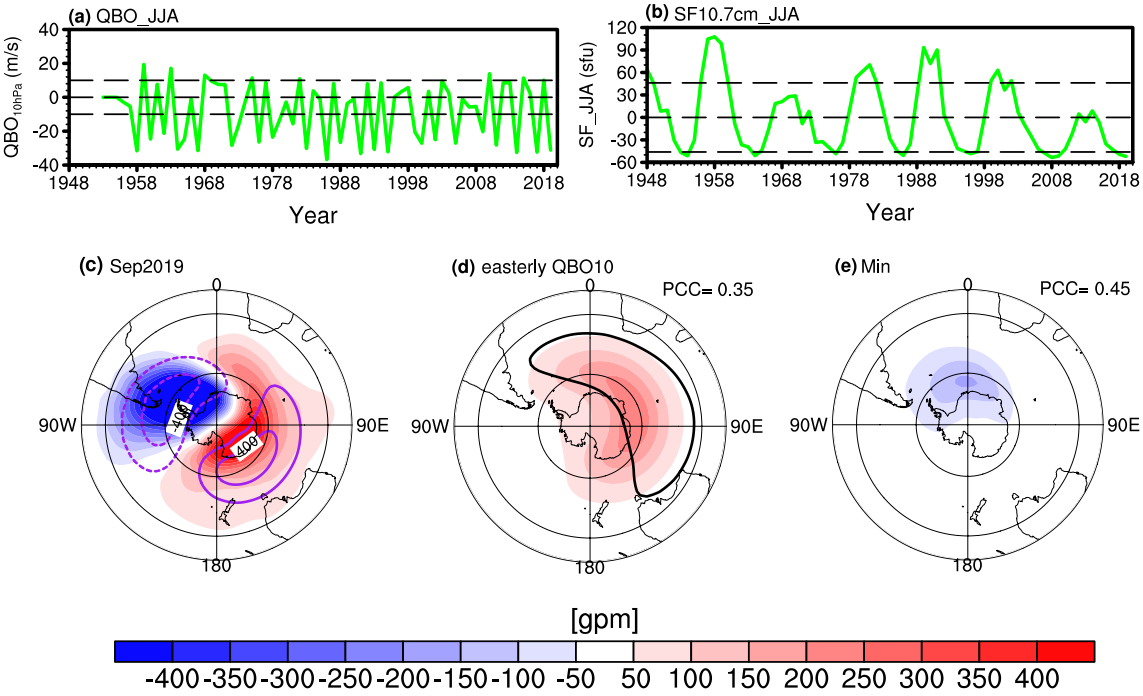

803

804 **Figure 3.** (a) Time series of the southern winter-mean QBO index at 10 hPa (units: m/s). The
805 top and bottom reference lines show the thresholds (±10 m/s) for westerly and easterly phases,
806 and the middle reference line is the zero wind. (b) Time series of the southern winter-mean
807 solar flux at 10.7 cm with the climatology removed. The top and bottom reference lines show
808 the thresholds (±1 standard deviation) for solar maxima and minima, and the middle reference
809 line is zero. (c) The geopotential height anomaly pattern at 10 hPa in September 2019. The
810 purple contours show the zonal deviation of the climatological geopotential height in
811 September at ±200 and ±400 gpm. (d, e) The composite geopotential height anomaly pattern
812 at 10 hPa in September following easterly QBO and solar minima, respectively. The black
813 contours show the composite height anomalies at the 95% confidence level based on the
814 Student's *t*-test. The pattern correlation coefficient between the observed anomaly pattern in
815 September 2019 and the composite anomaly pattern is also shown for easterly QBO at 10 hPa
816 and solar minima.

817

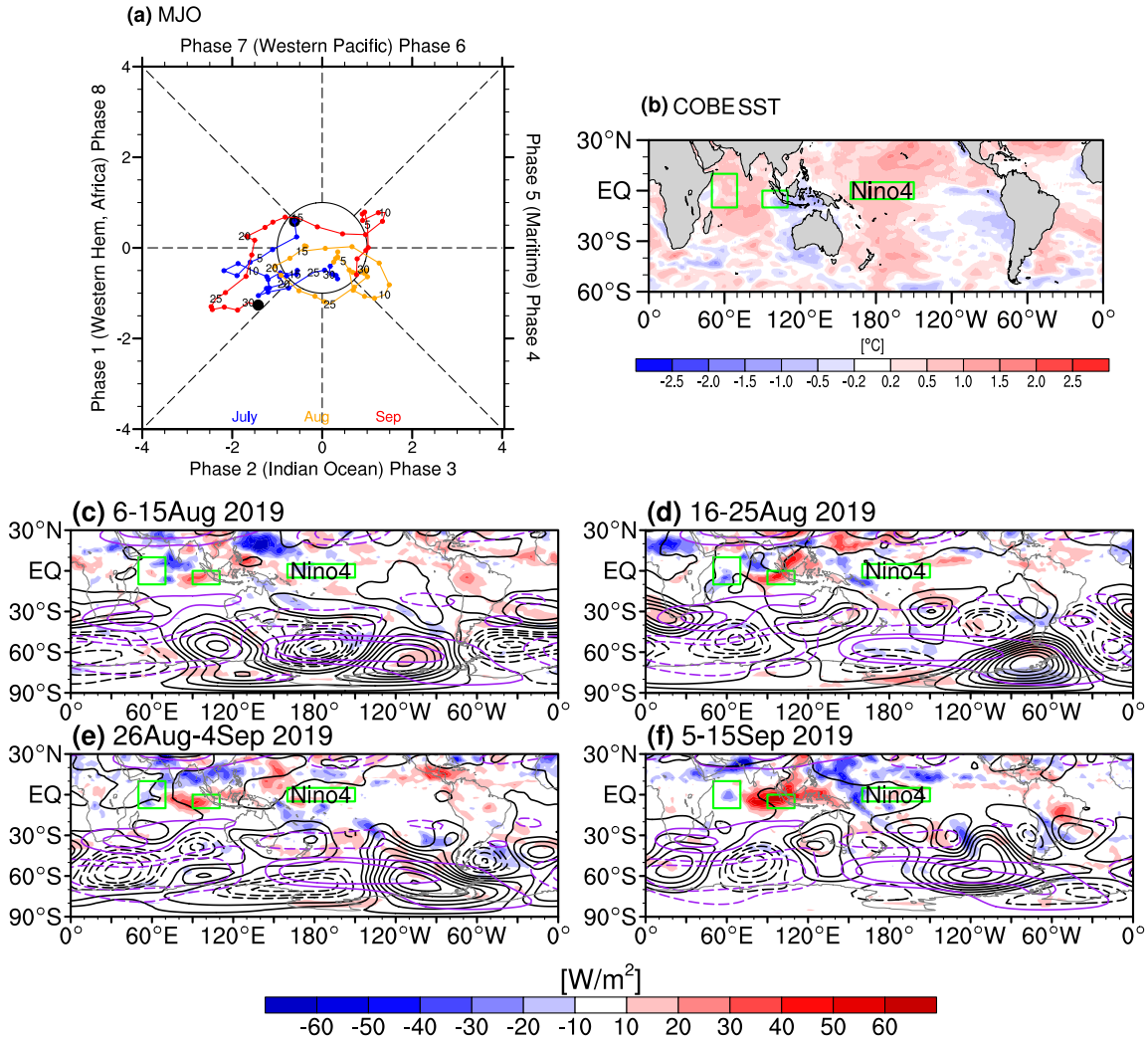

Figure 4. (a) Evolutions of the MJO amplitude and phase in July (blue), August (orange), and September (red) 2019. (b) The SST anomaly pattern in the 2019 southern winter (June–August). (c–f) Spatial patterns of OLR anomalies (shadings, units: W/m^2) and 200-hPa geopotential height anomalies (contours, units: gpm; interval: 40) in four sub-periods. The purple contours show the zonal deviation of the climatological geopotential height at ±40 and ±80 gpm. The green box in Pacific marks the Niño4 region (5°S–5°N, 160–210°E), and the green boxes (10°S–10°N, 50–70°E; 10°S–0°, 90–110°E) in the Indian Ocean mark the two key regions for the IOD.

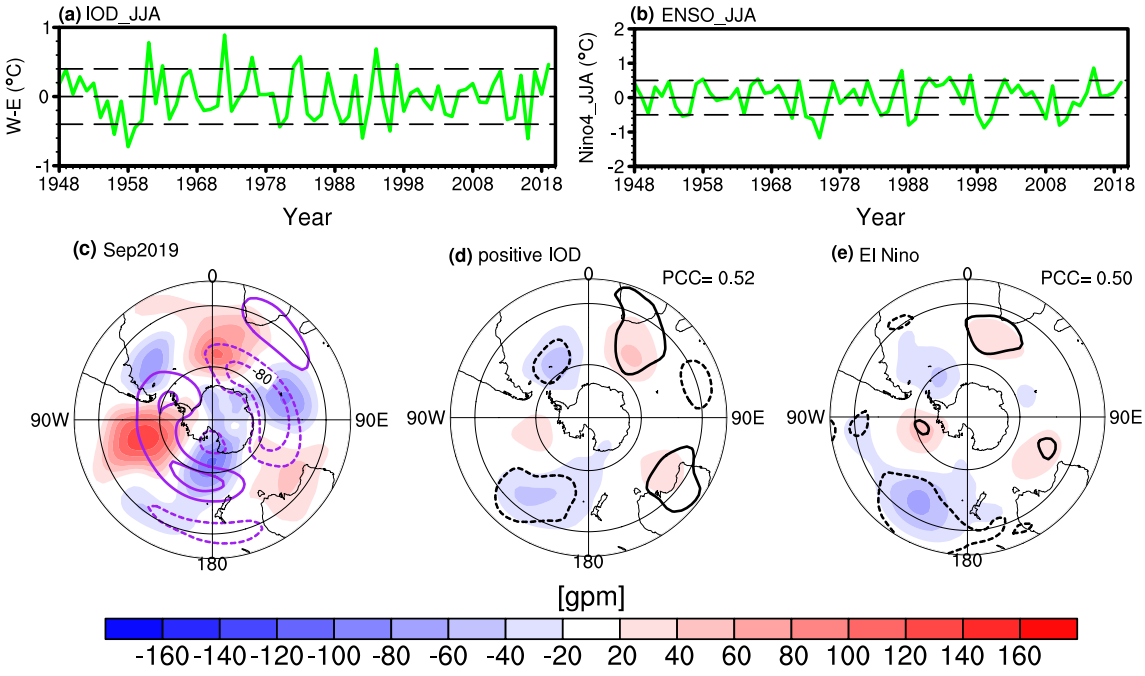

828

829 **Figure 5.** (a) Time series of the southern winter-mean IOD index (units: °C). The top and
830 bottom reference lines show the thresholds (±0.4 °C) for positive and negative IOD events, and
831 the middle reference line is zero. (b) Time series of the southern winter-mean Niño4 index
832 (units: °C). The top and bottom reference lines show the thresholds (±0.5 °C) for central Pacific
833 El Niño and La Niña events, and the middle reference line is zero. (c) The geopotential height
834 anomaly pattern at 500 hPa in September 2019. The purple contours show the zonal deviation
835 of the climatological geopotential height in September at ±40 and ±80 gpm. (d, e) The
836 composite geopotential height anomaly pattern at 500 hPa in September following positive
837 IOD and central Pacific El Niño events, respectively. The contours show the composite height
838 anomalies at the 95% confidence level. The pattern correlation coefficient between the
839 observed anomaly pattern in September 2019 and the composite anomaly pattern is also shown
840 for positive IOD and central Pacific El Niño events.

841

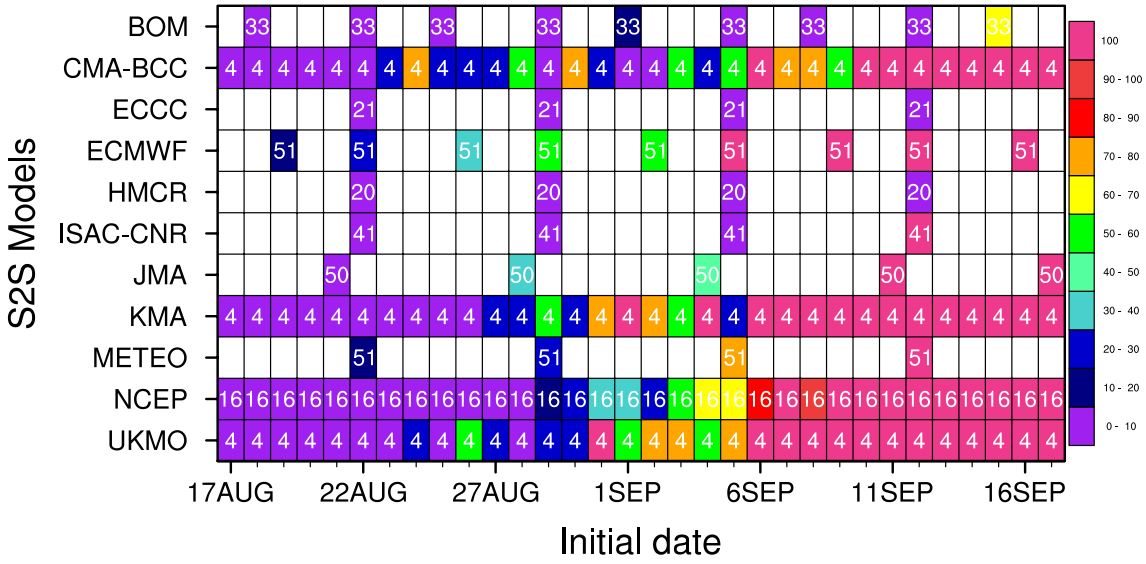

842

843 **Figure 6.** Distribution of ensemble member size (the number in each grid cell) in real-time
844 predictions for each initialization of the 11 S2S models from 17 August–17 September 2019.
845 The color shading denotes the hit ratio (units: %) of the ensemble members that forecast the
846 zonal-mean zonal wind at 60°N and 10 hPa falling below 20 m/s near 16 September 2019, with
847 a 2-day maximum error in timing allowed. Since the HMCR model does not provide
848 predictions at 10 hPa, the zonal mean zonal wind at 50 hPa is used to calculate the hit ratio.
849 The white unfilled grid denotes that the corresponding model did not initialize real-time
850 predictions on those dates.

851

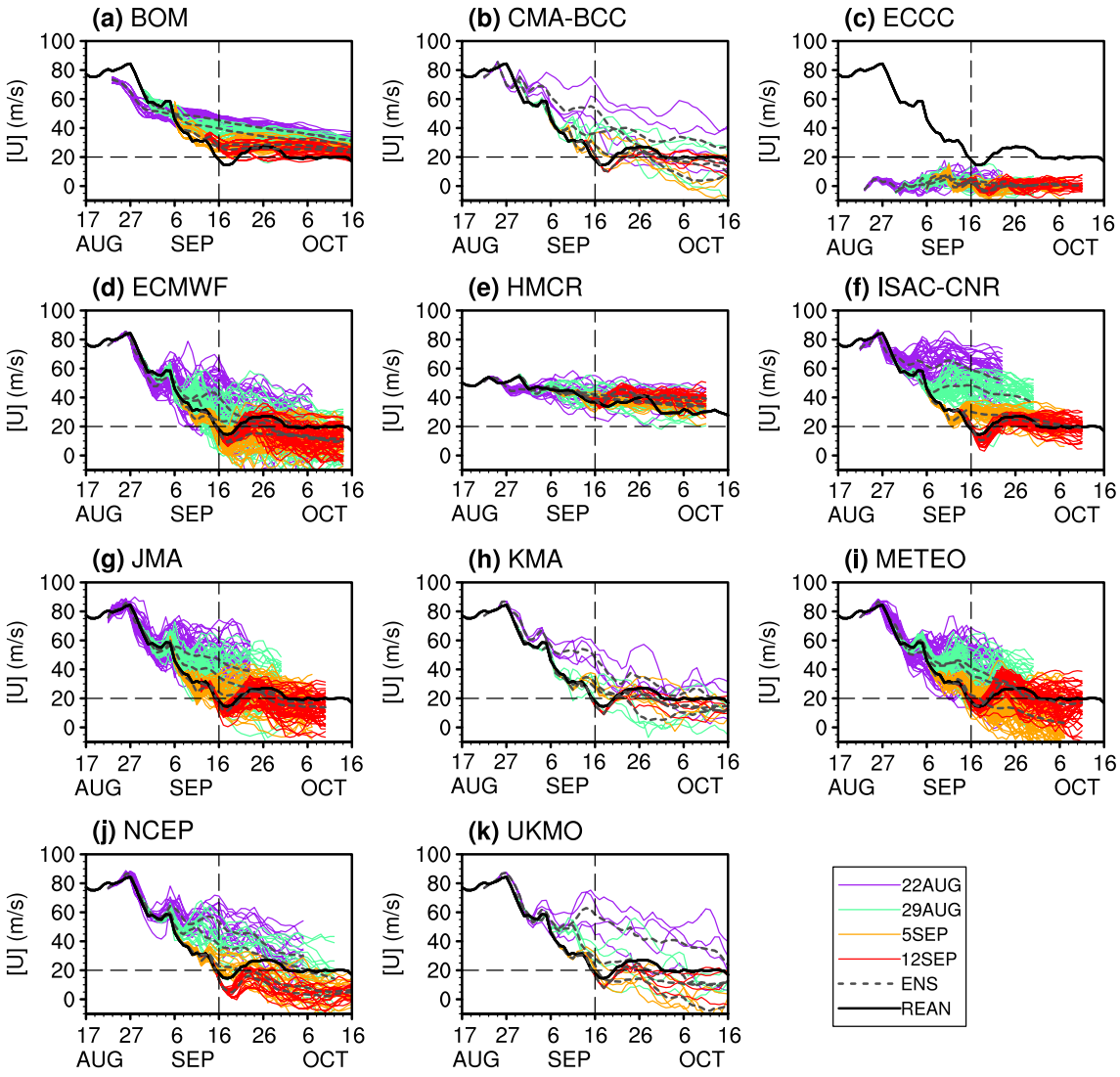

852

853 **Figure 7.** Real-time predictions of the zonal-mean zonal winds at 10 hPa and 60°S (units: m/s)
854 in the four common initializations (22, 29 August, and 5, 12 September 2019) by the 11 models.
855 The colors denote the initialization date. The gray dashed curves are the ensemble mean of the
856 forecasts initialized on the same date. The black curves are the reanalysis, shown for reference.
857 Note that JMA initialized its predictions one day earlier (21, 28 August, and 4, 11 September
858 2019; see Figure 6) than other models.

859

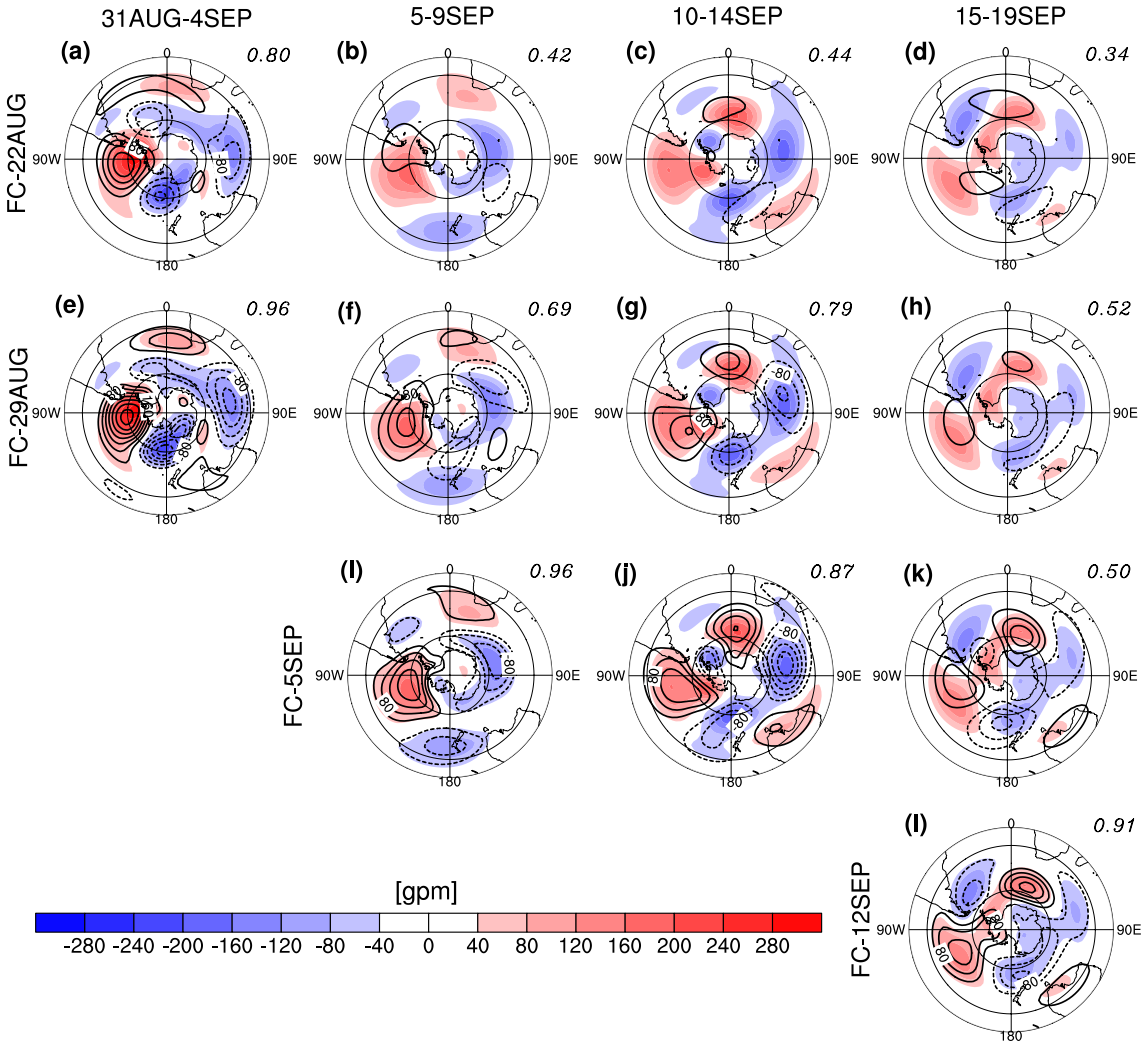

860

861 **Figure 8.** Eddy height anomalies (units: gpm) by zonal waves 1–3 at 500 hPa in the southern
862 extratropics during (first column) 31 August–4 September, (second column) 5–9 September,
863 (third column) 10–14 September, and (last column) 15–19 September from the multi-model
864 ensemble mean (MME) initialized on (top row) 22 August, (second row) 29 August, (third row)
865 5 September, and (last row) 12 September. The contours show forecasts from the MME
866 (contour interval: 40, zero skipped), and the shadings are the reanalysis. The pattern correlation
867 of eddy height anomalies between forecasts and reanalysis is also printed on the top right of
868 each plot.

869

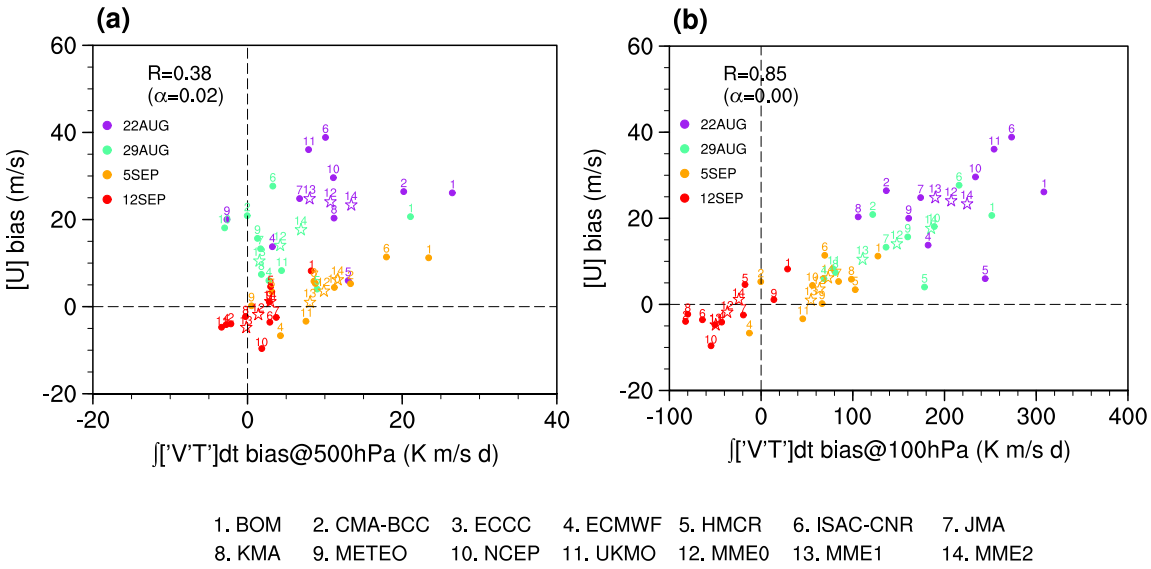

870

871 **Figure 9.** (a) Model-by-model scatterplot of the ensemble mean cumulative eddy heat flux bias
872 by wave-1 at 500 hPa during 7–16 September, averaged in the 45–75°S latitude band versus
873 the zonal-mean zonal wind bias at 10 hPa and 60°S during 16–20 September. The color denotes
874 the initialization date, and the number marks the model. The correlation (and its significance
875 level) between the cumulative eddy heat flux bias and zonal wind bias is also printed. (b) As
876 in (a) but for the scatterplot of the cumulative eddy heat flux bias at 100 hPa versus the zonal
877 wind bias at 10 hPa and 60°S. As an outlier, the ECCC model (#3) is excluded in the MME
878 and correlation calcuation. MME0 = MME for all models except ECCC (#1, #2, #4–#11);
879 MME1 = MME for high-top models (#4, #7, #8, #10, #11); MME2 = MME for low-top models
880 (#1, #2, #5, #6, #9).

881

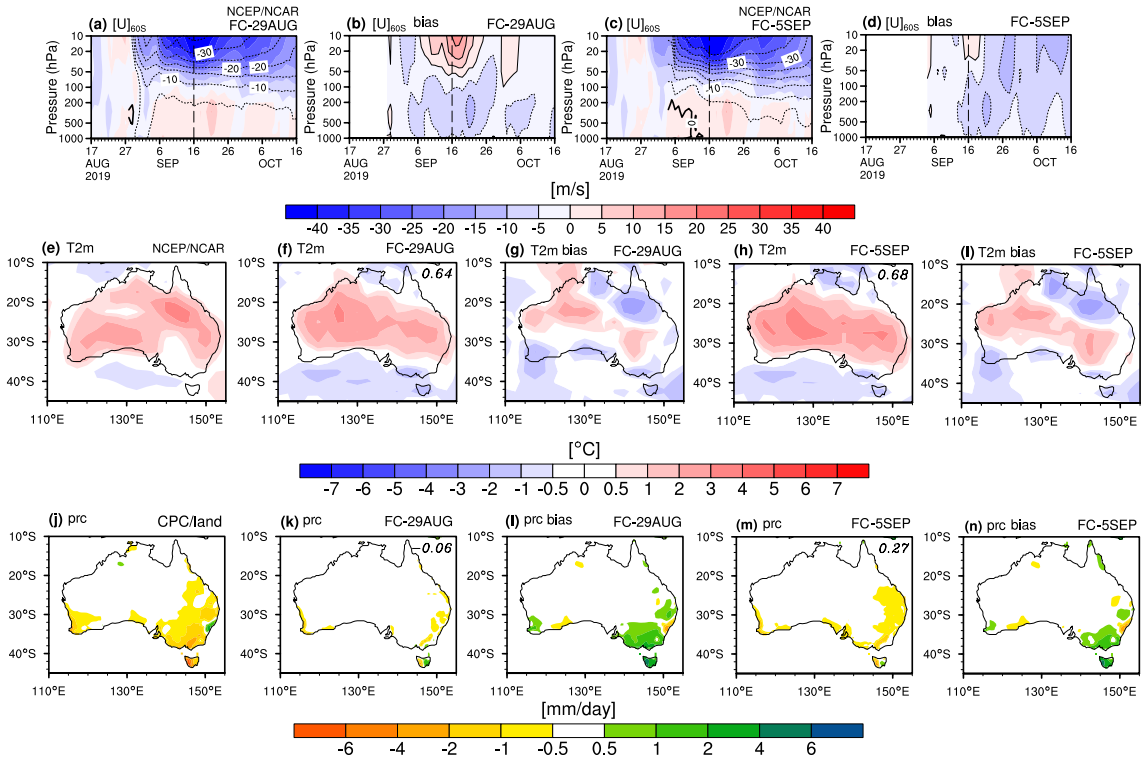

Figure 10. (a) Pressure-temporal evolutions of the zonal-mean zonal wind anomalies at 60°S in the MME (excluding ECCC) initialized on 29 August. The reanalysis is shown in shadings as reference, and the forecasts are shown in contours. (b) The forecasted zonal-mean zonal wind anomaly bias. (c, d) as in (a, b) but for the MME initialized on 5 September. (e) The 2-m temperature anomalies in the following two weeks (16–30 September) after the SSW onset from the reanalysis. (f) Forecasted 2-m temperature anomalies in the MME initialized on 29 August. (g) The prediction bias for the 2-m temperature anomalies in the MME initialized on 29 August. (h, i) As in (f, g) but for the MME initialized on 5 September. (j–n) As in (e–i) but for the precipitation observation and forecasts. The pattern correlation between the observation and forecasts is also show in the top right of the plot if applicable.